Supporting Information

Attomole-sensitive milk fever sensor using 3D-printed multiplex sensing structures

Section S1: Chemicals

Poly(3-octylthiophene-2,5-diyl) (POT), tetrahydrofuran (THF), polyvinyl chloride (PVC), sodium tetrakis[3,5-bis(trifluoromethyl)phenyl] borate, dioctyl sebacate (DOS), tributyltin chloride, 2-Nitrophenyl octyl ether (NPOE), calcium ionophore II, and Nafion were purchased from Sigma-Aldrich (St. Louis, MO, USA). Sodium phosphate dibasic (Na_2HPO_4), calcium chloride ($CaCl_2$), sodium chloride (NaCl), potassium chloride (KCl), Ag/AgCl ink (composed of finely dispersed chloritized silver flakes) were obtained from Fisher Scientific, Waltham, MA, USA**.** Deionized (DI) water having a resistivity of 18.2 MΩ.cm was obtained using a purification system from Millipore, US. The cocktail of the calcium-ion selective membrane (Ca–ISM) is composed of 33% polyvinyl chloride (PVC), 0.05% sodium tetrakis[3,5-bis(trifluoromethyl)phenyl] borate, 65% dioctyl sebacate (DOS) and 1% calcium ionophore II mixed with 660 µl of tetrahydrofuran per 100 mg of the weighted mixture.[1] This solution was sealed and stored at −4 °C. The cocktail of the phosphate-ISM is composed of 1% tributyltin chloride, 66% NPOE (2-nitrophenyl octyl ether), 33% polyvinyl chloride (PVC), 1% Sodium tetrakis[3,5 bis(trifluoromethyl)phenyl] borate 660 µl of tetrahydrofuran per 100 mg of the weighted mixture.[2] This solution was sealed and stored at −4 °C.

The high-temperature resin cartridge (V2) was bought from Dynamism, Inc., Chicago, IL, and is used to manufacture the sensor base.

Section S2: Ion Selectivity Evaluation

To evaluate the selectivity using the Nikolskii-Eisenman formalism, the logarithmic component in the equation (Eq. S1) can be replaced with a sum of activities adjusted by selectivity factors, as outlined in the following equation.

$$E = E_0 + \frac{RT}{zF} \ln(a_I + K_{IJ}^{p} a_J^{Z_I/Z_J}) \qquad \text{(Eq. S1)}$$

where K_{IJ}^{p} represents the selectivity coefficient, a_I and a_J stand for the activities of ions I and J in the test solution, and Z_I and Z_J denote the charges of the primary and interfering ions, respectively.

Section S3: Calculation of LOD

The limit-of-detection (LoD) is calculated in three steps as described in literature.[3,4]

$$\text{LoB} = \bar{x}_b + 1.645 \times \sigma_b \qquad \text{Eq. S2}$$

$$Y_{LoD} = \text{LoB} + 1.645 \times \sigma_l \qquad \text{Eq. S3}$$

$$\text{LoD} = \frac{Y_{LoD} - c}{m} \qquad \text{Eq. S4}$$

where σ_b, σ_l, $\bar{x}$, $\bar{x}_b$, c, m, LoB, and Y_{LoD} are standard deviation of blank sample, standard deviation at low concentration, sample mean, blank mean, intercept of the calibration equation, slope of the sensor calibration, Limit of Blank, and LoD of the signal, respectively.

For Ca-sensor, the calculation based on Eqs. (S2), (S3) and (S4) are:

$$\bar{x}_b = -0.1937 \text{ V}, \sigma_b = 0.0015 \text{ [}n\text{, replicate = 3]}$$

$$\text{LoB} = -0.1937 + 1.645 \times 0.0015 = -0.1912 \text{ V}$$

Mean signal at the lowest concentration (1 aM of calcium ion) is 0.0895 V, with a standard deviation of 3.87×10^{-4} V for [n, replicate = 3].

$$Y_{LoD} = -0.1912 + 1.645 \times 3.87 \times 10^{-4} = -0.1905 \text{ V}$$

The Ca–sensor calibration equation is Y_{LoD} (V) = 0.0243× log [X (mM)] + 0.122. Hence, the LoD of the Ca–sensor in calculated to be $10^{-12.86}$ mM or 138 aM of Ca^{2+} ions.

For P–sensor, the calculation based on Eqs. (S2), (S3) and (S4) are:

$$\bar{x}_b = 0.358 \text{ V}, \sigma_b = 0.00116 \text{ [}n\text{, replicate = 3]}$$

$$\text{LoB} = 0.358 + 1.645 \times 0.00116 = 0.3599 \text{ V}$$

Mean signal at the lowest concentration (10 μM of phosphate ion) is 0.335 V, with a standard deviation of 5.1×10^{-3} V for [n, replicate = 3].

$$Y_{LoD} = 0.3599 + 1.645 \times 5.1 \times 10^{-3} = 0.3582 \text{ V}$$

For P–sensor, the calibration equation is Y_{LoD} (V) = 0.152× log [X (mM)] + 0.341. Hence, the LoD of the calcium sensor in calculated to be 2.6 μM of P or PO_4^{2-} ions.

Section S4: **Instruments**

The morphology of sensor microstructures was scanned with a scanning electron microscopy (SEM, JEOL IT500 SEM). The elemental analysis (i.e. EDS) and mapping analysis of the sensor' materials were conducted using the Oxford Aztec EDS detector integrated into the SEM instrument. A 3D Solid work CAD design software was employed to generate a 3D design and schematic of the device depicted in Fig. S1 of the Supporting Information. The VersaSTAT 4 Potentiostat/Galvanostat from Princeton Applied Research-Ameteck, with VersaStudio software, was utilized to record and analyze Cyclic Voltammetry (CV), Electrochemical Impedance Spectroscopy (EIS), and Open Circuit Potentiometry (OCP) signals. For applications beyond the laboratory, the OCP was recorded using the portable EmStat3 Blue (PalmSens) Potentiostat/Galvanostat. During EIS measurements, the AC signal had a 1 mV amplitude and a frequency range of 10,000–1 Hz. All electrochemical analyses were conducted at room temperature.

Chromium and gold layers were deposited on the high-temperature resin sensor base substrates using an e-beam evaporator (PVD 250).

Lithography-free, 3D sensor was printed using an extrusion-based Form 3L 3D printer (FormLabs), followed by IPA washing with Form Wash L (FormLabs) and curing with UV light using Form Cure L (FormLabs). The AutoCAD software (AutoCAD 2022; Autodesk Inc.) was employed to design the 2D sensor and create CAD programming file to shadow mask. A Kapton tape-based shadow mask for the device was created using an automated cutter from Silhouette Curio™, Silhouette America®, Inc. Graphs and statistical analysis were generated using OriginPro 2023b and Graphpad prism software. All the graphical illustrations were generated using Biorender 2023 software.

Sensor design and real photograph of the device

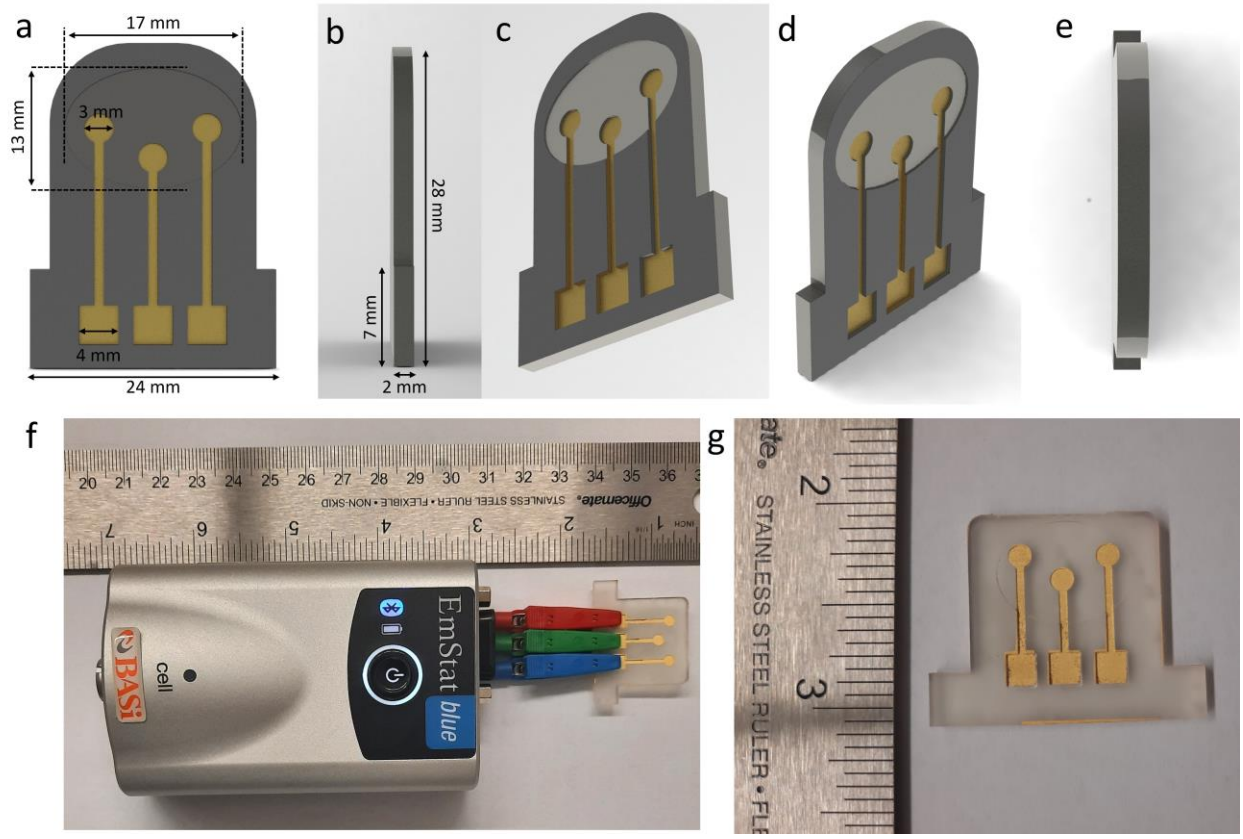

Fig. S1. Sensor design for manufacturing. (a) Front view of the sensor with dimensions. The diameter of each electrode is 3 mm and depth are 2 mm. An elliptical-shaped sample holder was created, and all three electrodes are placed onto the sample holder. (b) Side view of the sensor with dimensions. (c, d, e) Solid work designs of the 3D sensor from different angles. (f) A real photograph of the device showing overall size of the sensor. The sensor is connected with a Blue-tooth enabled portable potentiostat circuit to collect the data. (g) The printed sensor and its dimension showed after gold coating onto the electrodes.

Sensor morphological studies

The morphological investigation of the sensor geometry was conducted by SEM studies. The SEM images depicting POT-Au@3D Sensor (Fig. S2a-b) reveal the presence of a POT layer covering the gold-coated sensor base. This is a partial coverage to demonstrate the surface morphology. This coverage elucidates the observed decline in electrical conductivity as indicated in the cyclic voltammogram (Fig. 2f). The POT layer is responsible for this decrease the sensor conductivity due to the insulating nature of it. However, the POT layer is ideal to build a solid-state type of potentiometric sensor as the sensor doesn't flow current through it except develops the membrane potential. The coverage of POT was enhanced by increasing its concentration to develop sensors.

Fig. S2c-d shows the SEM images after coating ion-selective membrane on POT-Au layer. SEM images a seamlessly uniform surface of ISM, indicating that the membrane envelops the entire sensor surface along with the underlying micro-structures.

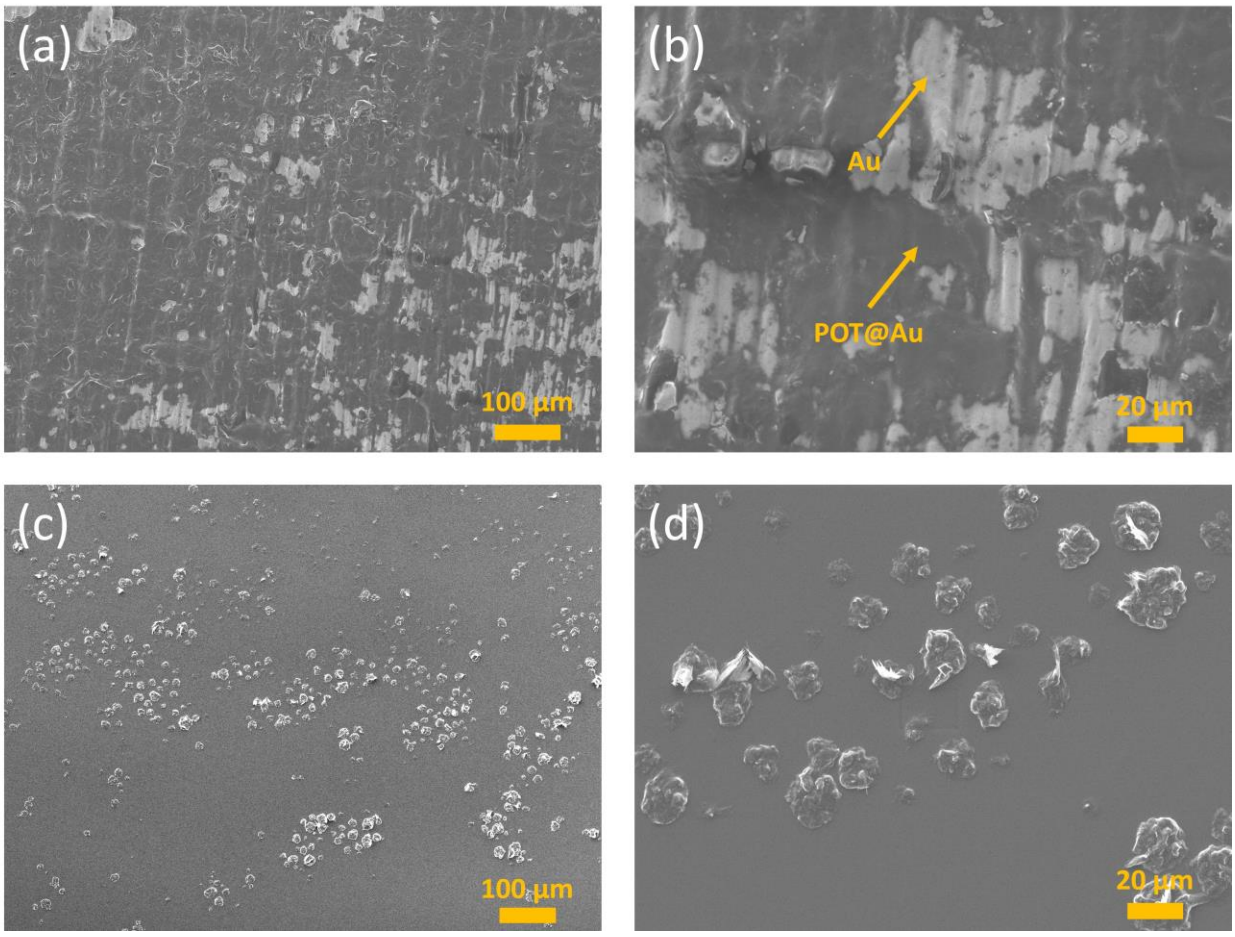

Fig. S2. The sensor morphological studies. SEM images of (a, b) POT-Au electrode, and (c, d) ISM coated POT-Au electrode. POT layer is covered partially the wrinkled Au surface. The ISM coating on POT-Au showed full coverage with a thick film formation. The full coverage of ISM is to prevent water entering into the POT layer during measurement, hence increase the selectivity of the sensor.

Estimation of geometrical variation within the sensor structures

We have conducted SEM analysis to assess the variation of sensor geometry featuring lateral patterns. We have chosen ten random points for measuring the thickness of the lateral layers, selected from various locations on both distinct and identical lateral structures. The width of average lateral layer was ~78.065 μm, accompanied by a standard deviation (SD) of ± 2.518 μm (Table S1 of the Supporting Information). This low deviation serves as a measure of the printer's accuracy in replicating micro-structures during the printing process. It is important to note that the combination of the sensor base's wrinkled structure and the lateral pattern micro-structure serves to amplify the sensor's surface area, thereby enhancing the analytical sensitivity of the sensor.

Table S1. Lateral distances (μm) of periodic printed layers of the 3D printed sensor.

Location	Lateral Distance (μm)	SD (μm)
No. 1	72.28	
No. 2	79.95	
No. 3	77.43	
No. 4	78.81	
No. 5	77.03	
No. 6	76.68	
No. 7	81.36	
No. 8	78.72	
No. 9	80.26	
No. 10	78.13	
Average	**78.065**	**± 2.518**

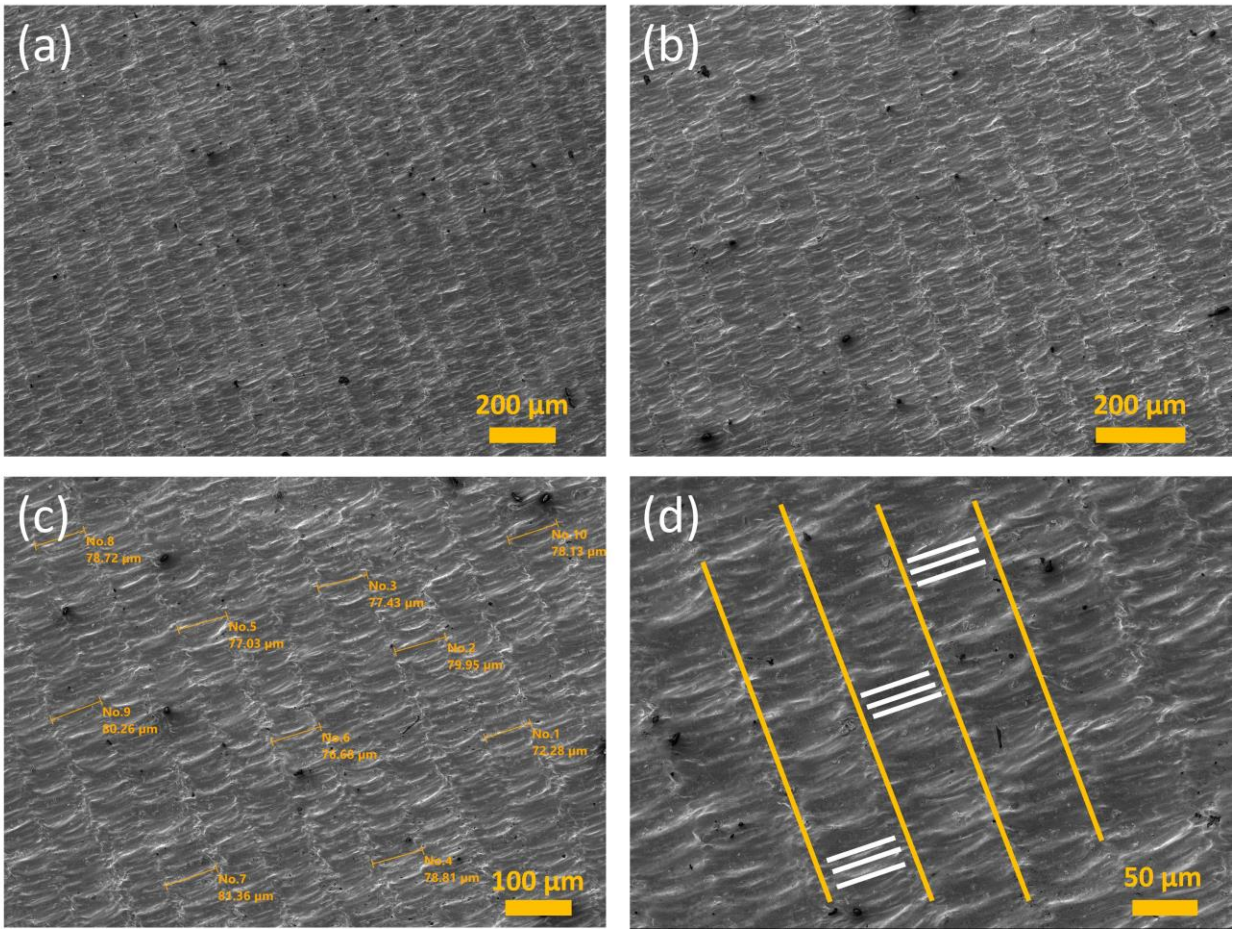

Fig. S3. Scanning Electron Microscopy (SEM) images of (a, b) the wrinkled structure of 3D printed sensor coated with 100 nm Au at different magnifications. (c) The SEM images of the 3D printed sensor and ten randomly selected points with ruler scale to calculate 3D printer's accuracy in printing sensor with micro-structure patterns. (d) SEM image indicating primary (lateral patterns – indicated in yellow line) and secondary (wrinkled structures – indicated in white line) patterns.

Energy dispersive spectroscopy analysis

Energy Dispersive Spectroscopy (EDS) technique was used to analyse the elemental composition of materials on each layer of the sensor. In EDS analysis, a sample is bombarded with electrons, causing it to emit X-rays characteristic of its elemental composition. These X-rays are then detected and used to identify the elements present in the sample and quantify their concentrations. We conducted EDS analysis on every layer of the sensor, namely Au, POT-Au, and ISM-POT-Au. The EDS graphs depicting the results can be found in Fig S4a, S4b, and S4c. The observed reduction in gold's surface weight percentage and the corresponding increase in carbon's surface weight percentage provide confirmation of the effective coverage of POT and ISM layers over the gold layer. Considering the reported electron beam penetration depth of approximately 10 µm at a potential of 20.0 kV on the sample surface,[5] and it can be inferred that the thickness of each POT and membrane layer exceeds 10 µm.

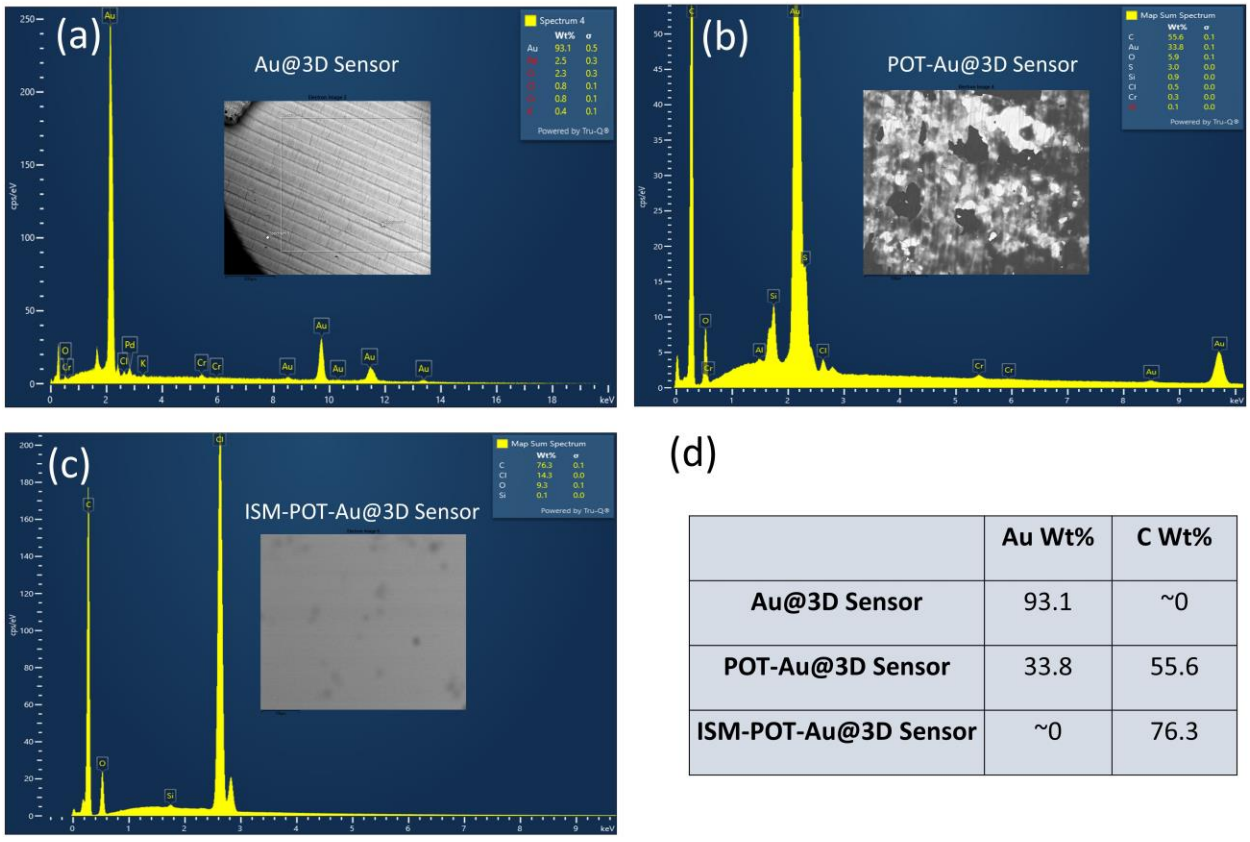

	Au Wt%	C Wt%
Au@3D Sensor	93.1	~0
POT-Au@3D Sensor	33.8	55.6
ISM-POT-Au@3D Sensor	~0	76.3

Fig. S4. Surface analysis of the sensor. EDS analysis of different sensor surfaces such as (a) Au@3D sensor, (b) POT-Au@3D sensor, (c) ISM-POT-Au@3D sensor are conducted to investigate the surface elemental components, and (d) A table detailed the weight % of gold and carbon for different layers of the sensors, which are expected to vary with the surfaces.

Elemental mapping analysis

The mapping results of the POT-Au@3D sensor (Fig. S5a) validate the existence of sulphur and carbon atop the gold layer, corresponding to poly(3-octyl-thiophene) (POT), which solely comprises carbon and sulphur. Additionally, the predominant constituent of the membrane is poly-vinyl chloride (PVC), identified through the mapping analysis of ISM-POT-Au@3D in Fig S5b, revealing the presence of carbon and chloride.

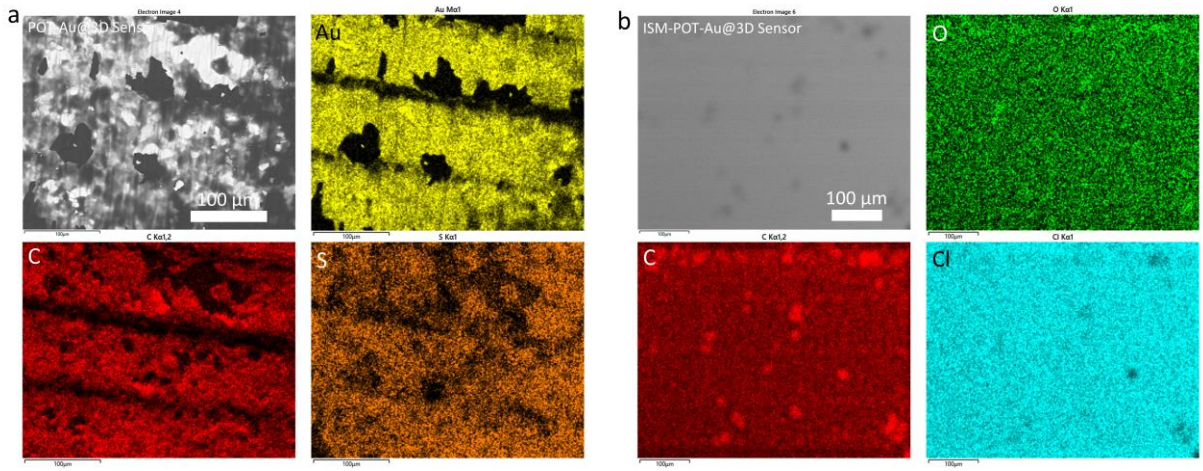

Fig. S5. Elemental mapping analysis of the sensor to confirm the before and after coating ISM on POT-Au electrode. Mapping of elemental compositions were indicated with specific colours. (a) POT-Au@3D sensor, (b) ISM-POT-Au@3D sensor.

X-ray photoelectron spectroscopy (XPS) analysis

X-ray Photoelectron Spectroscopy (XPS) was used to investigate the elemental composition and chemical state of materials. XPS provides detail information about the outermost atomic layers (up to 1-10 nanometers) of each layer of the sensor. By analysing the binding energies, XPS can identify the elements present on the surface of a material and provide information about their chemical bonding environments. In this regard, we have performed XPS survey analysis on 3D printed sensor base made of epoxy resin and the gold coated layer of the sensor. As indicated in Fig S6a, the XPS survey shows peaks characteristics of O1s, C1s, Si2s, Si2p, and O2s demonstrating the presence of oxygen, carbon, and silicon on the surface of freshly printed and cured epoxy resin 3D printed base. Carbon and oxygen are expected as these are the main constituent of epoxy resin, however, the presence of silicon is the minimal contamination of the sensor surface during the curing and washing process. Fig S6b also indicates the XPS survey results on gold coated 3D sensor base. As indicated in this figure, the main element identified on this surface is gold along with carbon and oxygen coming from negligible organic contamination on the surface.

The deconvoluted XPS result for the C1s peak in Fig S6c reveals distinct contributions from different carbon chemical states on the surface of 3D printed base. Three major peaks are identified at specific binding energies: the peak centred at 284.8 eV corresponds to C-C bonds, indicative of carbon-carbon interactions. The peak at 286.2 eV is attributed to carbon-oxygen (C-O) bonds, suggesting the presence of functional groups in epoxy resin. Furthermore, the peak at 289.0 eV is associated with the O-C=O configuration, characteristic of carbonyl groups.

Additionally in Fig S6d, slow XPS scan result for the O1s peak is shown. Three distinct peaks are observed at binding energies of 530.9 eV, 532 eV, and 529.1 eV. The peak at 530.9 eV is attributed to oxygen-carbon (O-C) bonds, indicating the presence of carbon-oxygen functionalities in the material. The peak at 532 eV signifies oxygen-hydrogen (O-H) bonds, indicative of hydroxyl groups on the surface. Lastly, the peak at 529.1 eV is associated with oxygen double-bonded to carbon (O=C), suggesting the presence of carbonyl groups.

Finally, high-resolution XPS scan conducted on a gold-coated 3D printed sensor base has revealed distinct peaks corresponding to the $Au4f_{7/2}$ and $Au4f_{5/2}$ binding energies, demonstrating the gold coating in its atomic state (Fig.6Se). The appearance of two satellite peaks at higher binding energies for each of these main peaks further enriches the spectral information obtained. In XPS analysis, the satellite effect is a phenomenon observed as additional peaks adjacent to the main photoelectron peaks, resulting from the relaxation process of the core hole created during the photoemission.

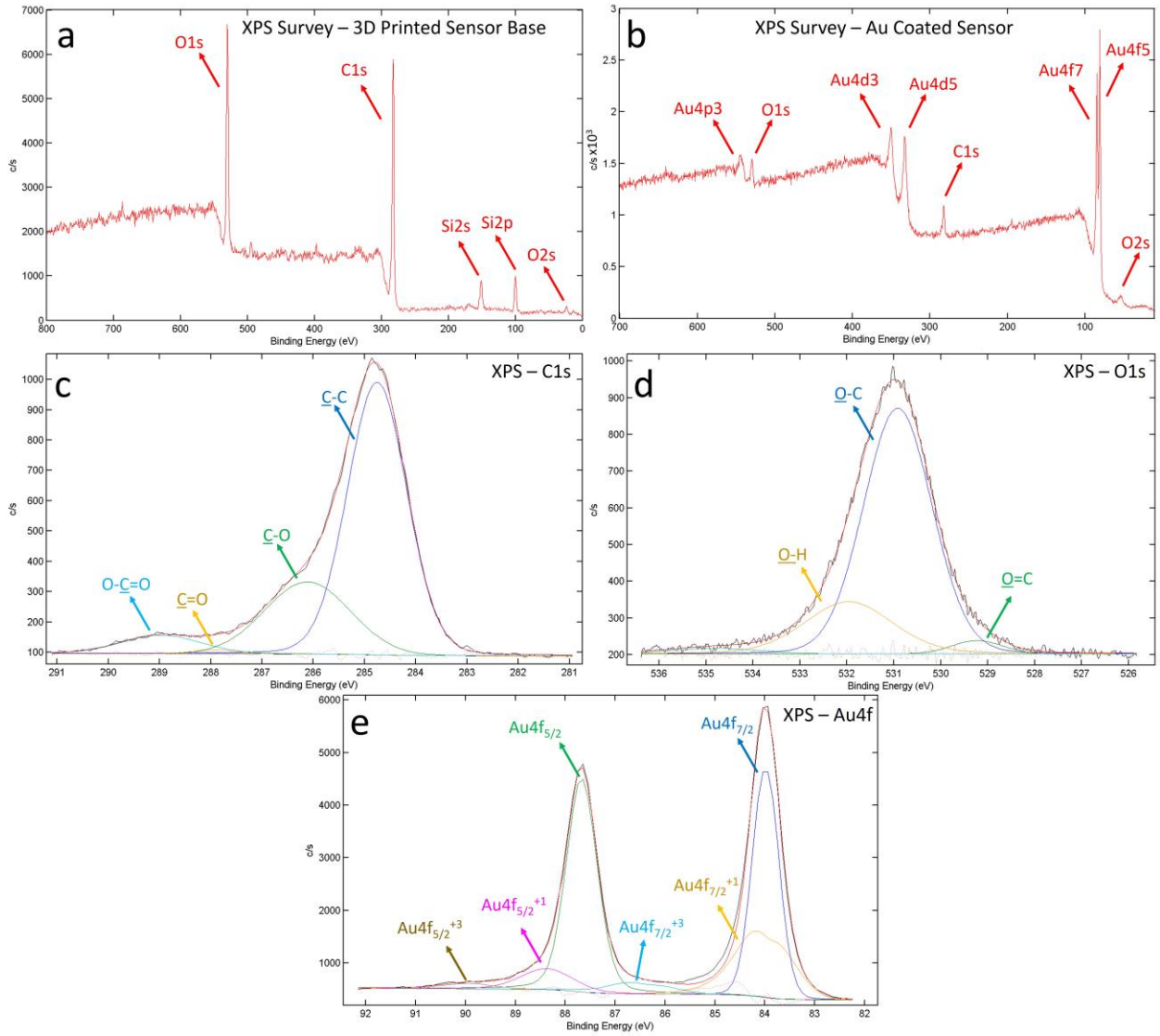

Fig. S6. X-ray Photoelectron Spectroscopy (XPS) analysis survey scan on (a) 3D printed sensor base made of UV cured epoxy resin, and (b) gold coated 3D printed sensor. Deconvoluted high resolution XPS scans of (c) carbon (C1s), (d) oxygen (O1s), and (e) gold (Au4f).

Real sample analysis data

Table S2. Milk sample analysis data for calcium ion measurements with both commercial and 3D printed sensors. Precision of the sensor (RSD) and accuracy of the sensor with average percentage of % 8.97.

Milk (lb)	DIM	Parturition	Sample Number	Ca-Sensor results in ppm	SD (ppm)	Ca-meter (commercial) results in ppm
114.2	22	Multiparous	1	125.02	6.53	110
103.7	48	Multiparous	2	145.50	4.98	130
112.9	43	Multiparous	3	134.49	6.77	150
128.5	68	Multiparous	4	155.63	4.39	150
123.1	28	Multiparous	5	146.82	5.86	160
149.9	38	Multiparous	6	140.21	2.38	140
116.1	31	Multiparous	7	137.79	3.76	150
-	12	Multiparous	8	146.82	0.65	130
129.7	50	Multiparous	9	154.74	3.68	140
-	5	Multiparous	10	161.79	6.62	180

Table S3. Milk sample analysis data for phosphate ion measurements with both commercial and 3D printed sensors. Precision of the sensor (RSD) and accuracy of the sensor with average percentage of % 5.53. All milk samples have been diluted for phosphate analysis.

Milk (lb)	DIM	Parturition	Sample Number	P- Sensor results in ppm (ppm)	RSD (%)	P-Sensor (commercial) (ppm)	Concentration Differences (ppm)	Difference Percentage (%)
-	12	Multiparous	11	1130.1	0.99	1000	130.1	13.01
-	13	Multiparous	12	1327.7	2.63	1250	77.7	6.216
129.7	50	Multiparous	13	1226.3	1.65	1250	23.7	1.896
-	5	Multiparous	14	1285.6	1.26	1250	35.6	2.848
103.7	32	Multiparous	15	1296.2	2.23	1250	46.2	3.696

Commercial Ca-meters calibration and performance

To enhance our comprehension and comparison of our proposed sensor with a commercial calcium ion sensor, we conducted a calibration of the commercial calcium meter using standard solutions ranging from 10 mM to 1M. The calibration equation revealed that the commercial meter adheres to the Nernst equation,

as indicated by a slope of +29.78 mV/dec matching the $0.0592/z_A$ (V/dec) term in the Nernst equation, where z_A represents the number of electrons in the electrochemical half reaction. Subsequently, we examined the meter's response to standard calcium solutions, following the company's recommendation to calibrate the meter using commercial solutions with concentrations of 150 ppm and 2000 ppm. In Fig. S7b, we presented the sensor calibration using provided standard solutions and showcased the sensor's response to standard solutions with concentrations of 80, 120, 160, 190, and 230 ppm. This concentration range was strategically chosen to encompass the calcium concentration found in cow's milk samples. The calibration graphs (depicted in red and blue) highlight a disparity in the response of the commercial sensors, particularly in the low concentration region where the calcium ion concentration in milk samples exists. We also subjected the commercial meter to testing with standard solutions, and its response in calcium ion detection is illustrated in Fig. S7c.

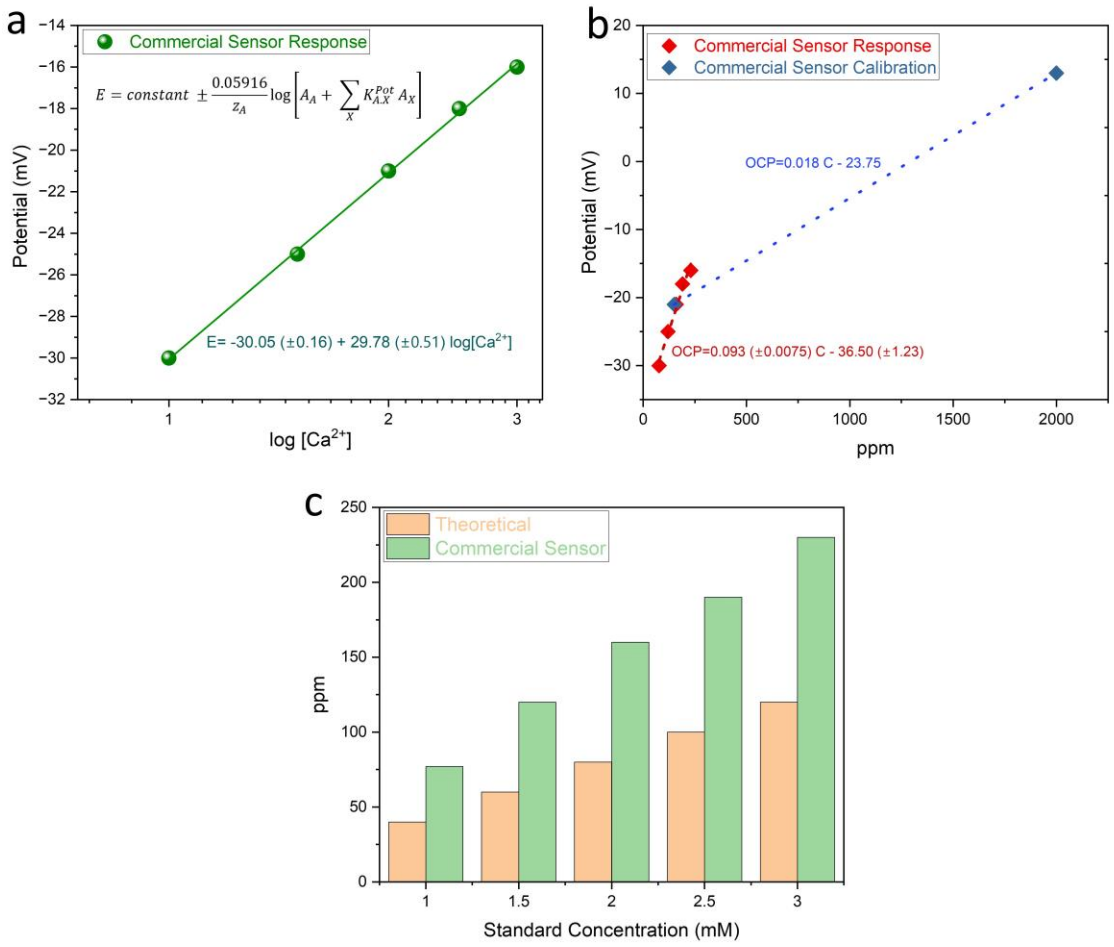

Fig. S7. (a) The calibration curve of a commercially available calcium ion meter and the associated calibration equation validate its adherence to the Nernst equation. The calibration process involved using standard calcium ion solutions ranging from 10 mM to 1M in concentration. (b) The calibration graph of the

commercial sensor exhibits two recommended product solutions for calibration at 150 ppm and 2000 ppm concentrations (depicted in the blue graph). Our experimentation involved testing the sensor with calcium ion standard solutions at concentrations of 80, 120, 160, 190, and 230 ppm (illustrated in the red graph). These concentrations were strategically chosen to encompass the calcium concentration range found in cow's milk samples. (c) The bar graph highlights the difference in the commercial sensor's response to standard calcium ion solutions. Notably, the meter tends to indicate higher calcium ion concentrations than the actual values, particularly in the low concentration range using for milk sample testing.

Optimization of POT layer

In this study, the POT or poly(3-octyl-thiophene) has utilized as a sensor material. The amount of POT concentration on the sensor surface was optimized. It is a conducting polymer acted as an ion-to-electron transducer layer and this layer converts signals between ions and electrons in this device. Consequently, demonstrating the impact of POT concentration on our proposed sensor's sensing capabilities is crucial. To investigate this, we constructed three identical Ca-sensors with varying amounts of POT layer and established calibration curves for each sensor (**Fig. S8, Supporting Information**). Three different amounts of POT such as 1.1 $\mu g/mm^2$, 2.2 $\mu g/mm^2$ and 3.6 $\mu g/mm^2$ were chosen for this study. This exploration aimed to understand the influence of POT on sensor performance and potentially optimize the POT concentration. Illustrated in **Fig. S8a, S8b,** and **S8c**, the calibration graphs exhibit nearly identical slopes (sensitivity), indicating that the transducer amount does not affect sensing performance. Interestingly, the superior sensing performance and lower detection limit of the sensor are attributed to the increased surface area of the wrinkled 3D printed sensor base, as evidenced. Based on these results, a thin layer of POT layer covering the sensor surface proves sufficient for providing high sensor performance.

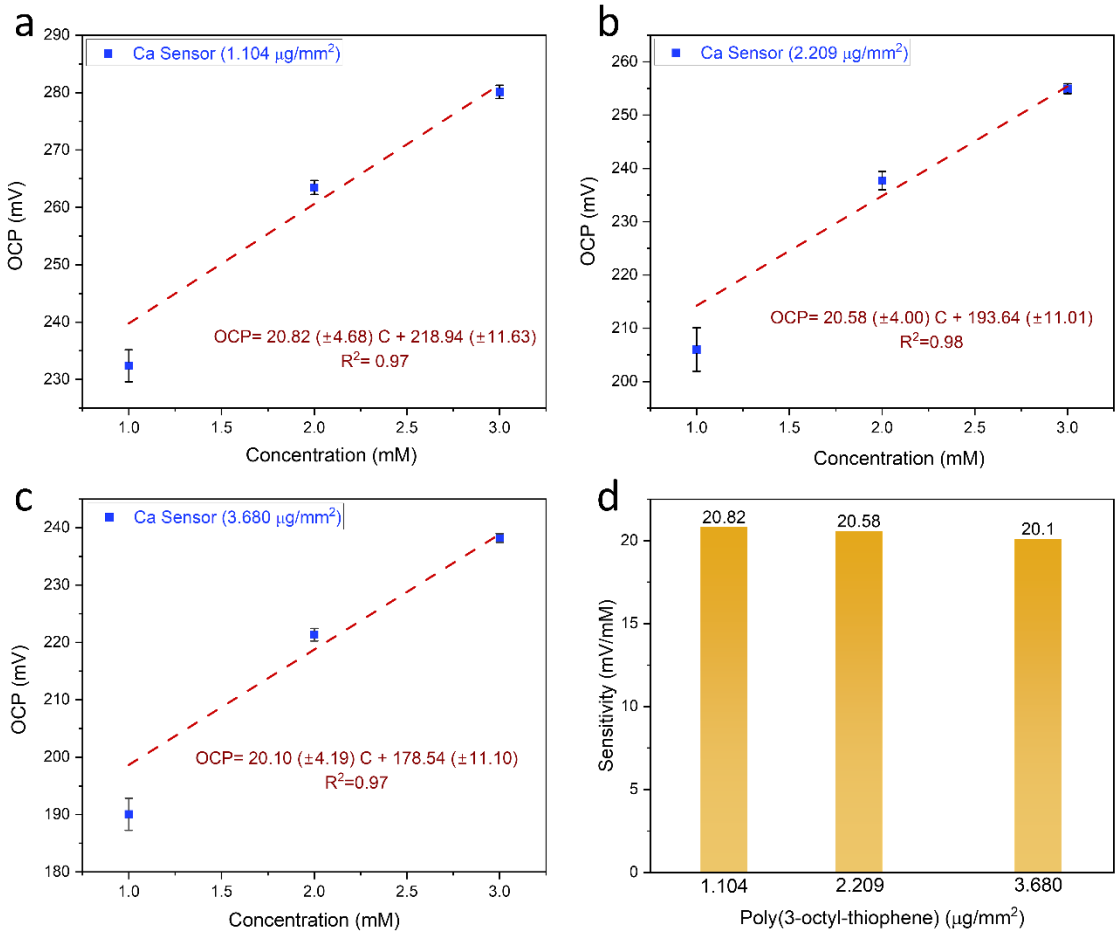

Fig. S8. Optimization of POT layer. For this study, we have chosen three identical sensors and modified with three different concentrations of POT solutions such as 1.1 µm/mm^2 (a), 2.2 µm/mm^2 (b) and 3.6 µm/mm^2(c). Calibration graphs of Ca–sensors fabricated with similar methods but with different concentrations of POT layer. (d) Bar graph compares the sensitivity of different sensors with different POT casted on the surface.

References

1 Nyein, H. Y. Y. *et al.* A Wearable Electrochemical Platform for Noninvasive Simultaneous Monitoring of Ca2+ and pH. *ACS Nano* **10**, 7216-7224 (2016). https://doi.org:10.1021/acsnano.6b04005

2 Jiang, H., Ali, M. A., Jiao, Y., Yang, B. & Dong, L. in *2017 19th International Conference on Solid-State Sensors, Actuators and Microsystems (TRANSDUCERS)*. 289-292.

3 Ali, M. A. *et al.* Sensing of COVID-19 Antibodies in Seconds via Aerosol Jet Nanoprinted Reduced-Graphene-Oxide-Coated 3D Electrodes. *Advanced Materials* **33**, 2006647 (2021). https://doi.org:https://doi.org/10.1002/adma.202006647

4 Armbruster, D. A., Tillman, M. D. & Hubbs, L. M. Limit of detection (LQD)/limit of quantitation (LOQ): comparison of the empirical and the statistical methods exemplified with GC-MS assays of abused drugs. *Clin Chem* **40**, 1233-1238 (1994).

5 Zarraoa, L., González, M. U. & Paulo, Á. S. Imaging low-dimensional nanostructures by very low voltage scanning electron microscopy: ultra-shallow topography and depth-tunable material contrast. *Scientific Reports* **9**, 16263 (2019). https://doi.org:10.1038/s41598-019-52690-9